The Journal of Physical Chemistry Letters

Letter

Cite This: J. Phys. Chem. Lett. 2017, 8, 6211−6219

pubs.acs.org/JPCL

Controllable Synthesis of Two-Dimensional Ruddlesden−Popper-Type Perovskite Heterostructures

Jun Wang,[†,#] Junze Li,[†,#] Qinghai Tan,[‡,§] Lei Li,[†] Jianbing Zhang,[†] Jianfeng Zang,[†,∥] Pingheng Tan,[‡,§] Jun Zhang,*[,‡,§] and Dehui Li*[,†,⊥]

[†]School of Optical and Electronic Information, Huazhong University of Science and Technology, Wuhan 430074, China

[‡]State Key Laboratory of Superlattices and Microstructures, Institute of Semiconductors, Chinese Academy of Sciences, Beijing 100083, China

[§]College of Materials Science and Optoelectronic Technology, University of Chinese Academy of Sciences, Beijing 101408, China

[∥]Innovation Institute, Huazhong University of Science and Technology, Wuhan 430074, China

[⊥]Wuhan National Laboratory for Optoelectronics, Huazhong University of Science and Technology, Wuhan 430074, China

Supporting Information

ABSTRACT: Two-dimensional Ruddlesden−Popper type perovskites (2D perovskites) have recently attracted increasing attention. It is expected that 2D perovskite-based heterostructures can significantly improve the efficiency of the optoelectronic devices and extend the material functionalities; however, rational synthesis of such heterostructures has not been realized to date. We report on a general low-temperature synthetic strategy for the synthesis of 2D perovskite-based lateral and vertical $(n\text{-}CH_3(CH_2)_3NH_3)_2PbI_4/(n\text{-}CH_3(CH_2)_3NH_3)_2(CH_3NH_3)Pb_2I_7$ heterostructures for the first time. A combination of solution synthesis and gas−solid phase intercalation approach allows us to efficiently synthesize both lateral and vertical heterostructures with great flexibility. X-ray diffraction, photoluminescence, and photoluminescence excitation mapping and electrical transport measurement studies reveal the successful synthesis of lateral and vertical heterostructures with precisely spatial-modulation control and distinguishable interfaces. Our studies not only provide an efficient synthetic strategy with great flexibility, enabling us to create 2D perovskite-based heterostructures, but also offer a platform to investigate the physical processes in those heterostructures.

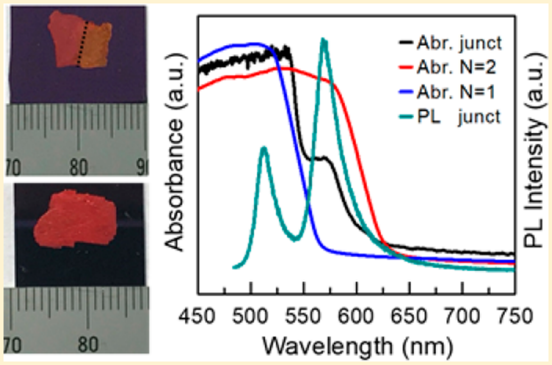

Hybrid organic−inorganic perovskites have undergone unprecedented rapid development recently as potential high-efficiency, low-cost solution-processable optoelectronic materials.[1−4] We have witnessed a rapid surge of the power conversion efficiency of the perovskite solar cells to a certified efficiency >20% within a few years due to the large absorption coefficient,[4] modest charge mobility,[5] and long carrier diffusion length of the perovskite materials.[6] In addition to the excellent performance in perovskite solar cells, the perovskite-based photodetectors, lasers, and light-emitting devices also have been demonstrated with fairly decent performance.[2,7,8] However, despite the rapid advancement of the perovskite-based optoelectronic applications, their extreme instability against moisture, light, and heat severely limits the perovskite materials to be commercialized.[9,10]

Compared with 3D perovskite mentioned above, the newly emerging 2D Ruddlesden−Popper type perovskites exhibit great environmental stability and possess natural quantum wells and thus have attracted increasing attention recently.[11−13] The general formula of 2D perovskites is $(A)_2(CH_3NH_3)_{N-1}M_NX_{3N+1}$, where A is a primary aliphatic or aromatic alkylammonium cation acting as a spacer between the perovskite layers, M is a divalent metal, X is a halide anion, and N is positive integer and represents the number of $[MX_6]^{4-}$ octahedral layers between two layers of A spacer cations. Because their band gap can be readily tuned via chemical composites and N values, 2D perovskites exhibit abundant and tunable optoelectronic properties and might find promising applications in solar cells,[11] LEDs,[14] photodetectors,[15] and lasers.[16] To date, most studies have been focused on bulk thin films, in which the presence of abundant grain boundaries would affect the performance of electronic and optoelectronic devices.[12,16,17]

Heterostructures integrate two or more materials with different energy landscape into one composite system. Heterostructures with increasing complexity not only provide a platform to study the new physical phenomena inaccessible to the single-material systems but also offer an additional degree

Received: October 26, 2017
Accepted: December 11, 2017
Published: December 11, 2017

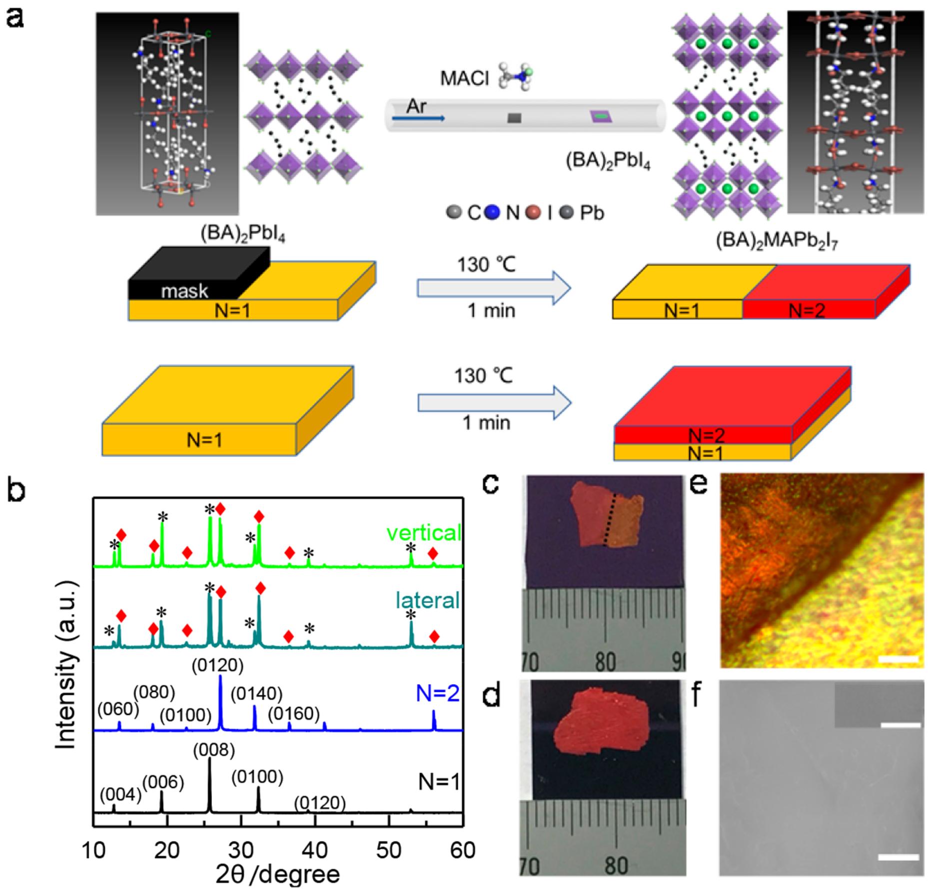

Figure 1. Material characterizations of 2D perovskite-based heterostructures. (a) Schematic illustrations of crystal structure of (BA)$_2$PbI$_4$(N = 1)/(BA)$_2$MAPb$_2$I$_7$(N = 2) and the gas−solid phase intercalation process to synthesize the lateral and vertical heterostructures. The crystal structures for N = 1 and N = 2 are monoclinic and orthorhombic, respectively. For gas−solid phase intercalation approach, MACl/MAI was used as precursor, reacting with the centimeter-size N = 1 plate, which was put at the downstream of the tube. For the synthesis of the N = 1/N = 2 lateral heterostructures, the as-grown N = 1 plate was partially covered by using a shadow mask. (b) XRD patterns of N = 1, N = 2 by solution method and lateral and vertical N = 1/N = 2 heterostructures by gas−solid phase intercalation method. Both the lateral and vertical heterostructures contain (00k) peaks of N = 1 and (0k0) peaks of N = 2, confirming the formation of the heterostructures. (c,d) Pictures of the lateral and vertical N = 1/N = 2 heterostructures. The dotted line in panel c represents the boundary of lateral heterostructures, whereas the yellow color portion and red color portion represent N = 1 and N = 2 2D perovskites, respectively. (e) Optical microscopy (OM) image of the lateral N = 1/N = 2 heterostructures. The scale bar is 20 μm. The relatively blur image for yellow color side of N = 1 is due to the different height of the surface from N = 2 after intercalation. (f) Scanning electron microscopy (SEM) image of the lateral N = 1/N = 2 heterostructures. The scale bar is 30 μm. The inset is a magnified SEM image which shows flat surface. The scale bar of the inset image is 3 μm.

of freedom to control charge-carrier transport and recombination processes for electronic and optoelectronic applications.[18−22] Thus rational design and synthesis of heterostructures are extremely important to fully explore their potential applications. The III−V- and II−VI-group-based heterostructure families[23] and recently heterostructures or multiheterostructures based on graphene and other 2D layered materials[24,25] have been extensively studied for field-effect transistors,[26] quantum-well lasers,[27] room-temperature magnetoresistance,[28] and light-emitting diodes (LEDs).[29] Whereas the large-scale III−V- and II−IV-group-based heterostructures are usually epitaxially grown by using molecular beam epitaxy and metal−organic vapor phase epitaxy, which are very expensive and usually operate at ultrahigh vacuum or high temperature,[30] the 2D-material-based heterostructures are fabricated by mechanical exfoliation and alignment transfer[31] or chemical vapor deposition method,[32] for both of which the size of samples is confined to be less than tens of micrometers, thus limiting their applications. We report on a general low-temperature synthetic strategy for efficient synthesis of 2D perovskite-based lateral and vertical heterostructures with great simplicity and flexibility.

Figure 1a displays the schematic illustrations of crystal structures of (n-$CH_3(CH_2)_3NH_3)_2PbI_4$ (denoted as (BA)$_2$PbI$_4$ or N = 1, where BA = n-$CH_3(CH_2)_3NH_3^+$) and (n-$CH_3(CH_2)_3NH_3)_2(CH_3NH_3)Pb_2I_7$ (denoted as (BA)$_2$MAPb$_2$I$_7$ or N = 2, where MA= $CH_3NH_3^+$). Closely inspecting the crystal structure of N = 1 and N = 2, the 2D perovskite crystals can be regarded as the inorganic layers of corner-sharing $[PbI_6]^{4-}$ octahedra sandwiched by two layers of BA spacer cations, while the methylammonium group $CH_3NH_3^+$ is inserted into the center of eight lead halide octahedrons for $N \geq 2$ and without $CH_3NH_3^+$ for N = 1. Therefore, we design a combination of solution synthesis and gas−solid-phase intercalation approach to obtain the 2D perovskite heterostructures.

To create 2D perovskite-based heterostructures, the centimeter-size N = 1 2D perovskite plates are first synthesized via naturally cooling a saturated solution of mixed hydroiodic acid, BAI, and PbI$_2$ from 140 °C to room temperature[11,12]

DOI: 10.1021/acs.jpclett.7b02843
J. Phys. Chem. Lett. 2017, 8, 6211−6219

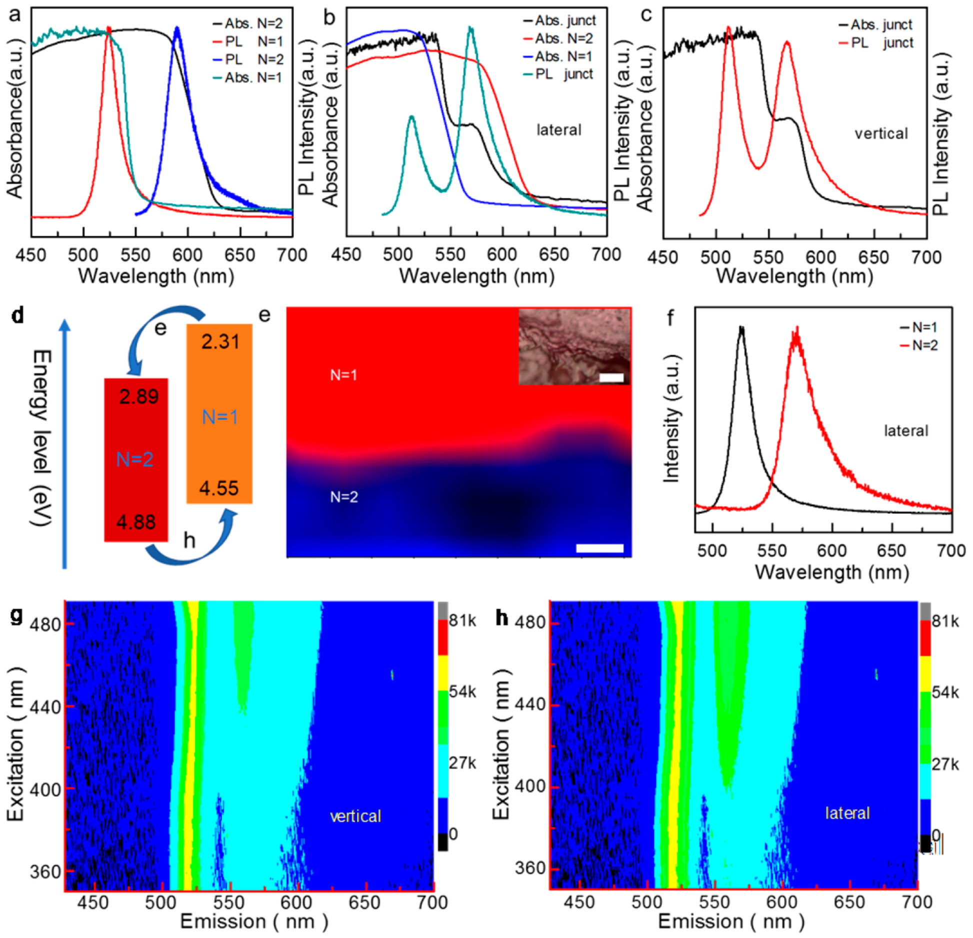

Figure 2. Optical properties of 2D perovskite heterostructures. (a) Normalized absorption and PL spectra of $N = 1$ and $N = 2$ plates obtained by solution method at room temperature. For the PL measurement, the excitation laser is 442 nm with a power density of 1 μW. (b, c) Normalized absorption and PL spectra of lateral and vertical $N = 1/N = 2$ heterostructures, respectively. Comparing with $N = 1$ and $N = 2$ by solution method in panel a, the absorption edges and emission peaks for the junction regions blue-shift from 590 to 570 nm for $N = 2$ and from 521 to 514 nm for $N = 1$. (d) Comparative energy band diagram of $N = 1$ and $N = 2$. (e) PL mapping image of the junction regions of a lateral N1/N2 heterostructure. Insert is OM image of the junction region. The scale bar is 2 μm. (f) PL spectra extracted from $N = 1$ and $N = 2$ regions in panel e. (g, h) Photoluminescence excitation intensity mapping as a function of both excitation and emission photon energies for (g) vertical and (h) lateral heterostructures.

(Experimental Section and Figure S1). This solution synthesis method enables us to obtain a large amount of $N = 1$ plates with excellent crystalline quality, as demonstrated by X-ray diffraction (XRD), photoluminescence (PL), and absorption spectra (Figures 1b and 2a). Then, the as-synthesized $N = 1$ plates are further converted into $N = 2$ 2D perovskites via a gas−solid-phase intercalation process under methylammonium iodide (MAI) vapor or methylammonium chloride (MACl) vapor by using high-purity Ar gas as carrier gas in a home-built chemical vapor deposition (CVD) system[33−35] (see Figure 1a and Experimental Section). During the intercalation process, the methylammonium ion is inserted into the center of eight octahedrons and the equatorial halide atoms are relocated while possibly two BAI molecules (MAI as precursor) or one BAI and one BACl (MACl as precursor) molecule are released away. Figure 1a provides the schematic illustration of the synthetic processes. For the synthesis of $N = 1/N = 2$ vertical heterostructures, the as-grown $N = 1$ 2D perovskite plates are simply put at the downstream, while we use a shadow mask to partially cover the as-grown $N = 1$ 2D perovskite plates to prevent them from being contacted with MAI/MACl vapor such that $N = 1/N = 2$ lateral heterostructures are obtained. It should be noted that this gas−solid intercalation method provides a very efficient and flexible way to produce $N = 2$ 2D perovskites and $N = 1/N = 2$ 2D perovskite lateral and vertical heterostructures at a relatively low temperature of ∼130 °C.

Figure 1c, d displays the picture of resultant centimeter-size $N = 1/N = 2$ lateral and vertical heterostructures, respectively. A clear color contrast between left and right sides (Figure 1c) indicates the formation of lateral heterostructures with the boundary outlined by a black dotted line, where yellow color portion and red color portion represent $N = 1$ and $N = 2$ 2D perovskite, respectively. A piece of Si substrate was used as mask in our experiments, and thus the shape of the junction is a straight line. For the vertical $N = 1/N = 2$ heterostructure, the entire surface has been converted to $N = 2$ 2D perovskite, and thus the red color of $N = 2$ 2D perovskite is able to be observed (Figure 1d). Nevertheless, the backside of the vertical $N = 1/N = 2$ heterostructure still maintains the yellow color, revealing the presence of $N = 1/N = 2$ junction within the plate (Figure S2). The X-ray diffraction patterns of both lateral and vertical heterostructures only contain the (00k) peaks of $N = 1$ and (0k0) peaks of $N = 2$ without other unassigned peaks,[12] confirming the phase purity and high-crystalline quality of the

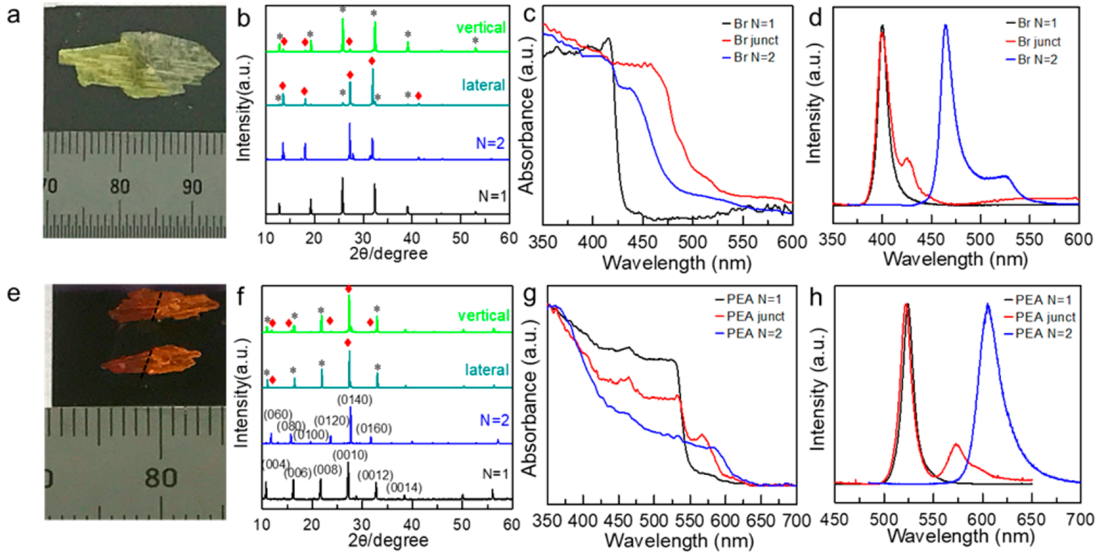

Figure 3. Structural and optical properties of $(BA)_2PbBr_4/(BA)_2MAPb_2Br_7$ and $(PEA)_2PbI_4/(PEA)_2MAPb_2I_7$ 2D perovskite heterostructures. (a, e) Pictures of lateral (a) $(BA)_2PbBr_4/(BA)_2MAPb_2Br_7$ and (e) $(PEA)_2PbI_4/(PEA)_2MAPb_2I_7$ heterostructures. The dotted lines in pictures show the boundary between $N = 1$ and $N = 2$ 2D perovskite. (b, f) XRD patterns of $N = 1$ and $N = 2$ obtained by solution method, (b) $(BA)_2PbBr_4/(BA)_2MAPb_2Br_7$, and (f) $(PEA)_2PbI_4/(PEA)_2MAPb_2I_7$ heterostructures by gas−solid phase intercalation method. The black asterisks represent the peaks belong to $N = 1$ and the red rhombus represent the peaks belong to $N = 2$. (c, g) Absorption spectra of (c) $(BA)_2PbBr_4/(BA)_2MAPb_2Br_7$ and (g) $(PEA)_2PbI_4/(PEA)_2MAPb_2I_7$ lateral heterostructures. (d, h) PL spectra of (d) $(BA)_2PbBr_4/(BA)_2MAPb_2Br_7$ and (h) $(PEA)_2PbI_4/(PEA)_2MAPb_2I_7$ lateral heterostructures. The peak at 530 nm in panel d is due to the emission from $MAPbBr_3$.

as-grown $N = 1/N = 2$ 2D perovskite heterostructures obtained by the synthetic strategy we developed. For comparison, we include the XRD diffraction patterns for pure $N = 1$ and $N = 2$ 2D perovskites synthesized by solution method (see Experimental Section). The optical image of lateral $N = 1/N = 2$ heterostructure enables us to closely inspect the details of the junction formed between $N = 1$ and $N = 2$ 2D perovskite, which exhibits two regions with strikingly different optical contrast separated by a nearly straight line and different thickness due to the shrinkage of the $N = 2$ side after intercalation (Figure 1e). The scanning electron microscope (SEM) image (Figure 1f) of the $N = 1/N = 2$ lateral heterostructure indicates that the surface of the resultant heterostructures becomes relatively rough, similar to perovskite microplates grown by vapor intercalation method[33] (Figure S3). In contrast, the zoom-in SEM image shows that the local surface of the resultant heterostructure is rather smooth, which would be beneficial for microelectronic and microoptoelectronic devices. Energy-dispersive X-ray (EDX) analysis reveals that the atomic ratio of the solution-processed $N = 2$ 2D perovskite is consistent with that of $N = 2$ portion in both lateral and vertical $N = 1/N = 2$ heterostructures produced by our gas−solid-phase intercalation method, which further confirms the successful formation of $N = 1/N = 2$ heterostructures (Figure S4 and Table S1). The absence of Cl element within the resultant heterostructures using MACl as precursor source proves the release of BACl during the intercalation process.

We have further characterized the optical properties of the resultant $N = 1/N = 2$ 2D perovskite heterostructures by PL and photoluminescence excitation (PLE) mappings. Figure 2a shows the room-temperature UV−vis absorption spectra of the $N = 1$ and $N = 2$ centimeter-size plates synthesized by solution approach for comparison. The band edges locate at 520 and 590 nm, consistent with the reported exciton energies of the $N = 1$ and $N = 2$ 2D perovskite films,[36,37] respectively. It should be noted that we did not observe the distinguished excitonic absorption peak due to the rather thick plates we used that the absorption is completely saturated above the excitonic absorption peak. The emission peaks of the room-temperature photoluminescence spectra (Figure 2a) of the solution processed $N = 1$ and $N = 2$ 2D perovskite plates are consistent with their absorption spectra and thus can be assigned to the free-exciton emission. To check whether the optical properties of the $N = 1$ and gas−solid intercalated $N = 2$ 2D perovskite are preserved, we acquired the absorption and PL spectra from $N = 1$ portion and $N = 2$ portion of the lateral $N = 1/N = 2$ 2D perovskite heterostructures. Both the absorption edges and emission peaks of $N = 1$ and $N = 2$ of the lateral heterostructures are consistent with those of $N = 1$ and $N = 2$ plates produced by solution method, indicating that the low-temperature gas−solid intercalation preserves the crystal structures of $N = 1$ and $N = 2$ 2D perovskites (Figure 2b and Figure S5). Nevertheless, compared with $N = 1$ and $N = 2$ 2D perovskites, both the absorption edges and emission peaks show blue shifts at the junction regions. At the junction regions, the absorption edge and the emission peak of $N = 2$ blue-shift around 80 meV from 590 to 570 nm, while those of $N = 1$ blue-shift around 30 meV from 521 to 514 nm (Figure 2b). The similar blue shifts were also observed for the vertical $N = 1/N = 2$ 2D perovskite heterostructures (Figure 2c). The observed blue shifts of absorption edge and emission peaks at the junction region have been reported in other heterostructures or quantum-well structures, which might be due to the strain originating from the lattice mismatch between monoclinic $N = 1$ and orthorhombic $N = 2$ 2D perovskites[38,39] or the quantum confinement effect arising from the formation of small nanocrystals during the conversion processes.[40,41]

In addition to the blue shift of the absorption edges and emission peaks at the junction region, the emission intensity of the junction region for both lateral and vertical $N = 1/N = 2$ 2D perovskite heterostructures significantly decreases compared

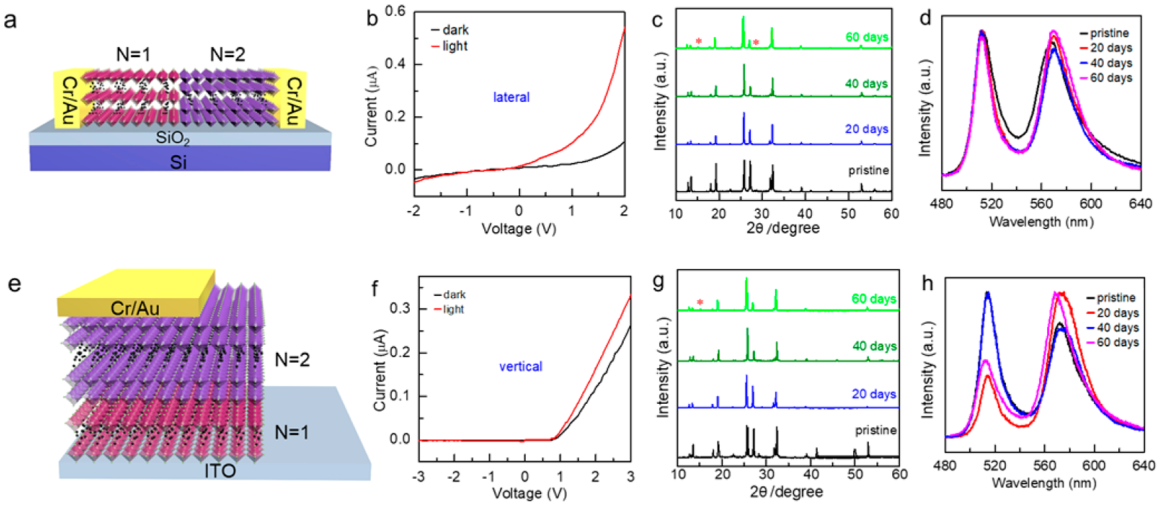

Figure 4. Electrical measurement and stability properties of the as-grown lateral and vertical heterostructures. (a, e) Schematic illustrations of the $(BA)_2PbI_4/(BA)_2MAPb_2I_7$ (a) lateral and (e) vertical heterostructure devices. 5 nm Cr/50 nm Au electrodes were deposited on $N = 1$ and $N = 2$ regions near the junction for lateral heterostructure device, while ITO was used as the bottom electrode and 5 nm Cr/50 nm Au electrode as the top electrode in the vertical heterostructure device. (b, f) Output characteristics (I versus V) of the (b) lateral and (f) vertical heterostructure devices in dark and under illumination (1.4 mW/cm^2). (c, d, g, h) Time evolution of XRD patterns and PL spectra for lateral (c, g) and vertical (d, h) heterostructures. The lateral and vertical heterostructures were stored under ambient conditions.

with that of $N = 1$ and $N = 2$ regions (Figure S6). Similar results also have been observed in the MoS_2/WS_2,[42] $MoS_2/MoSe_2$,[43]and $MoSe_2/WS_2$[44] van der Waals heterostructures. Such PL quenching might originate from the spatial charge separation due to the band alignment. On the basis of a previous report,[11] we are able to draw the band alignment diagram for $N = 1/N = 2$ 2D perovskite heterostructures (Figure 2d), which shows that the produced $N = 1/N = 2$ heterostructures belong to type-II structures. In such heterostructures, the photogenerated electrons prefer to move to $N = 2$ side while the holes transfer to $N = 1$ side, resulting in the PL quenching at the junction region. However, such band-alignment-induced photogenerated electrons and holes transfer in the opposite direction can enhance the carrier separation and efficient carrier extraction, which is thus beneficial for solar cells and photodetectors.[45,46]

To further check the spatial uniformity of the as-grown lateral $N = 1/N = 2$ heterostructures, the PL mapping was carried out in a typical lateral heterostructure (Figure 2e). We also carried out the PL mapping measurement for the vertical structures, in which the emission region of $N = 1$ and $N = 2$ is completely overlapped. For easier comparison, we plotted the PL mapping images both at 570 nm (corresponding to emission from $N = 2$ 2D perovskite, see Figure 2f) and at 514 nm (corresponding to emission from $N = 1$ 2D perovskite, see Figure 2f) into Figure 2e, which confirms the spatial modulation and formation of the heterostructures, agreeing well with the optical image of the junction. In addition, PLE mappings of both lateral and vertical $N = 1/N = 2$ 2D perovskite heterostructures further confirm the formation of the heterostructures (Figure 2g, h and Figure S7). For both lateral and vertical heterostructures, the excitation with higher energy leads to a blue shift of the emission peak and relatively stronger emission for $N = 1$ compared with that of $N = 2$. Further investigations are required for clarifying the underlying mechanism.

To demonstrate that our synthetic approach is versatile for a wide range of 2D perovskites other than $(BA)_2MA_{N-1}Pb_NI_{3N+1}$, we synthesized other types of 2D perovskite as examples: replacing I by Br and replacing BA by PEA ($PEA = C_6H_5C_2H_4NH_3^+$). Both lateral and vertical $(BA)_2PbBr_4/(BA)_2MAPb_2Br_7$ and $(PEA)_2PbI_4/(PEA)_2MAPb_2I_7$ heterostructures with centimeter size are successfully produced by applying the same procedure we developed to obtain $(BA)_2PbI_4/(BA)_2MAPb_2I_{7.}$ Figure 3a,e displays the pictures of the as-synthesized $(BA)_2PbBr_4/(BA)_2MAPb_2Br_7$ and $(PEA)_2PbI_4/(PEA)_2MAPb_2I_7$ heterostructures with centimeter size and strikingly different color between left and right side compared with the samples before gas−solid phase intercalation (Figure S8), confirming the formation of the lateral heterostructures.[47,48] XRD spectra show that all diffraction peaks of those two types 2D perovskite lateral and vertical heterostructures belong to their respective $N = 1$ and $N = 2$ components, indicating the phase purity and excellent crystalline quality of the resultant heterostructures. For comparison, we also show the XRD pattern of $(BA)_2PbBr_4$ and $(BA)_2MAPb_2Br_7$ in Figure 3b and $(PEA)_2PbI_4$ and $(PEA)_2MAPb_2I_7$ in Figure 3f, all of which are synthesized by solution method (see Experimental Section). The absorption spectra and PL spectra are examined to further confirm the formation of heterostructures (Figure 3c, d, g, h). Similar to the $(BA)_2PbI_4/(BA)_2MAPb_2I_7$ heterostructures, the absorption band edges and emission peak positions of $(BA)_2PbBr_4/(BA)_2MAPb_2Br_7$ and $(PEA)_2PbI_4/(PEA)_2MAPb_2I_7$ lateral structures exhibit a blue shift at the junction region. PL intensity at the junction region is also significantly quenched (Figure S9), which can be attributed to the photogenerated carrier transfer in type-II band alignment similar to $(BA)_2PbI_4/(BA)_2MAPb_2I_7$ heterostructures. The successful synthesis of $(BA)_2PbBr_4/(BA)_2MAPb_2Br_7$ and $(PEA)_2PbI_4/(PEA)_2MAPb_2I_7$ proves that the combination of solution and gas−solid vapor intercalation approach is general to produce lateral and heterostructures based on other types of 2D perovskites.

The centimeter size of the as-synthesized heterostructures allows us to fabricate electronic devices with shadow mask to

DOI: 10.1021/acs.jpclett.7b02843
J. Phys. Chem. Lett. 2017, 8, 6211−6219

evaluate the quality of the junctions. Figure 4a, d presents schematic illustrations of two-probe devices for the lateral and vertical $(BA)_2PbI_4/(BA)_2MAPb_2I_7$ heterostructures, respectively. For the vertical heterostructure device, we transferred the as-grown heterostructure to an indium−tin-oxide (ITO) substrate where ITO acts as the bottom electrode, while the 5 nm Cr/50 nm Au top electrode was defined by shadow mask and e-beam evaporation, which was adopted to fabricate the electrodes for lateral heterostructures on a 300 nm SiO_2/Si substrate with a channel length of ∼100 μm (Figure S10). The current−voltage characteristics of both $N = 1$ and $N = 2$ perovskite plates show a slight nonlinearity, indicating that the contact between our perovskites materials and Cr/Au electrodes is not optimal (Figure S11).

The current−voltage (I versus V) characteristics of both lateral and vertical $(BA)_2PbI_4/(BA)_2MAPb_2I_7$ heterojunction exhibit the diode behavior in dark, indicating the good quality of the as-grown junctions (Figure 4b, f). The PL spectra of the devices confirm that the heterostructures maintain the crystalline quality after the device fabrication (Figure S12). The vertical heterostructure device shows better rectification effect than that of lateral heterostructure device, which might be due to the imperfect interface within the lateral junction originated from the lattice mismatch between $N = 1$ and $N = 2$ 2D perovskites. The extracted rectification ratio (I_{on}/I_{off}) and the reverse current are around 750 at 2 V and 10.4 nA for vertical heterostructure and ∼160 at 2 V and 6.6 nA for lateral heterostructure, respectively. Upon light illumination (1.4 mW/cm^2 white light), the current increases for both lateral and vertical heterostructure devices. The photocurrents are evaluated to be 0.1 μA (at 3 V) for the vertical heterojunction and 0.4 μA (at 2 V) for lateral heterojunction, corresponding to the photoresponsivity of 2 and 8 A/W, respectively. With further optimizing the contact and device structure, we expect that much better performance can be achieved in our heterostructure devices.

By simply controlling the growth time or changing the precursor source, either $N = 1/N = 2$ vertical heterostructures with controllable junction depth or multiheterostructures with a mixed N-number phase can be synthesized. The conversion rate for MACl precursor is much larger than that for MAI as precursor source due to the smaller diameter of Cl atom. On the basis of this, we can controllably synthesize the multiheterostructures by properly selecting the precursor source and intercalation time. For instance, we used both MAI and MACl as precursor sources intercalating for 30 min to demonstrate the controllable synthesis of multiheterostructures. The XRD patterns show that the as-synthesized multiheterostructures contain peaks from $N = 2$ to $N = 4$ and rather weak peak from $N = \infty$ by using MAI as the precursor source while they contain peaks from $N = 2$ to $N = \infty$ when using MACl as the precursor[13] (Figure S13). The PL spectra of the as-synthesized products further confirm the formation of multiheterostructures with multiple emission peaks from $N = 2$ to $N = 4$ and $N = \infty$ for MAI precursor and $N = 2$ to $N = \infty$ for MACl precursor (Figure S14), consistent with the conclusion obtained from XRD spectra. It should be noted that we can precisely control to obtain $(A)_2\ MX_4/(A)_2(CH_3NH_3)\ M_2X_7$ heterostructures with pure N-number phase, while the junction depth cannot be well controlled in multiheterostructures, which are always consisted by mixed n-number phases for $N > 2$ due to the similar thermodynamic property for $N > 2$. In addition, we expect that $N = 1/N = 2$ lateral heterostructures with various patterns can be easily obtained by using shadow mask with different patterns.[49]

The major advantage for the emerging 2D Ruddlesden−Popper perovskites over 3D perovskites is their great environmental stability.[50,51] To check the stability of as-synthesized heterostructures, we have investigated the time evolution of the lateral and vertical $(BA)_2PbI_4/(BA)_2MAPb_2I_7$ heterostructures by using XRD technique. Similar to the 2D perovskites, the time evolution of XRD spectra (Figure 4c, g) indicates that the lateral and vertical $(BA)_2PbI_4/(BA)_2MAPb_2I_7$ heterostructures exhibit a good stability against the moisture, oxygen, and illumination. After being stored under ambient conditions for 60 days, only a small diffraction peak of PbI_2 is present, indicating the slight disintegration of the 2D perovskite and thus good stability compared with 3D perovskites, which usually decompose within several hours in ambient conditions. The good stability of our heterostructures is further confirmed by the time evolution of PL spectra (Figure 4d, h) and SEM images (Figures S15 and S16). No noticeable shift of PL peaks of the heterostructures is observed, and the surface of the heterostructures becomes slightly rough after being stored in ambient for 60 days.

In summary, we have demonstrated for the first time a simple and general synthetic strategy combining solution method and gas−solid phase intercalation to produce lateral and vertical 2D perovskite heterostructures with high efficiency, great controllability, and flexibility. XRD spectra, PL mapping, and absorption spectra reveal that the as-synthesized lateral and vertical heterostructures exhibit high crystalline quality, distinguishable interface, and great environmental stability. Electrical measurements indicate that both lateral and vertical heterostructures show good rectification behavior. By controlling the growth time and properly selecting the precursor source, we can obtain the heterostructures with controllable junction depth and multistructures with controllable spatial modulation. Our findings not only provide a general approach to controllably synthesize the large-scale 2D perovskite-based lateral and vertical heterostructures or multiheterostructures for fundamental research and potential optoelectronic applications but also open the way to preparing the heterostructures and multiheterostructures based on 2D perovskites.

■ EXPERIMENTAL SECTION

Synthesis of MACl/MAI/BAI/PEAI. The precursor MACl/MAI was synthesized by dropped methylamine (40 wt % in H_2O) into HCl (32 wt % in H_2O)/HI (57 wt % in H_2O) aqueous solution with a molar ratio of 1:1 and maintained at 0 °C with strong stirring for 2 h. The solvent was then evaporated at 60 °C and was washed by cold diethyl ether three times, followed by drying at 70 °C for 12 h. For synthesis of BAI (PEAI) solution, the same procedure was used, except that the methylamine was replaced by n-butylamine (phenethylamine) and the stirring time was extended to 4 h.

Synthesis of Centimeter-Size 2D Perovskite Plates by Solution Method. 0.5 g PbO powder was dissolved in a mixture of 3 mL of HI (57 wt % in H_2O) and 0.5 mL of H_3PO_2 (50 wt % in H_2O) by heating to 140 °C under magnetic stirring. Then, 2.5 mmol BAI solution was added to the resultant solution for the synthesis of $(BA)_2PbI_4$ plates while 1.25 mmol MACl solution and 1.75 mmol BAI solution were successively injected to the resultant solution for the synthesis of $(BA)_2MAPb_2I_7$ plates. Afterward, the stirring was stopped, and the solution was left to naturally cool to room temperature from 140 °C within ∼30 min, corresponding to a cooling rate of 4 °C/min. When the temperature decreases to 70 °C, the nucleation of the crystal immediately starts. With the further decrease in the temperature, the size of the crystal gradually increased. The precipitation was left to stand overnight for the growth to be completed.

For the synthesis of $(BA)_2PbBr_4$ and $(BA)_2MAPb_2Br_7$ ($(PEA)_2PbI_4$ and $(PEA)_2MAPb_2I_7$) 2D perovskite plates by solution method, the exactly same procedures were adopted except replacing the 57% w/w aqueous HI solution (BAI solution) with 48% w/w aqueous HBr solution (PEAI solution).

Synthesis of Lateral and Vertical Heterostructures by Gas−Solid Phase Method. For the growth of the vertical heterostructures, a quartz boat with MACl (MAI) precursor source was placed at the center of the tube furnace, while a piece of 300 nm SiO_2/Si substrate with centimeter-size $(BA)_2PbI_4$ ($(BA)_2PbBr_4$ and $(PEA)_2PbI_4$) plates obtained by solution method was placed at the downstream of the quartz tube. After the quartz tube was pumped down to a base pressure of 2 mTorr, a carrier gas of 60 sccm Ar was introduced. Then, the furnace was heated to 130 °C for MACl precursor and 140 °C for MAI precursor within 10 min and kept at this temperature for 1 min. Finally, the tube furnace was naturally cooled to room temperature with Ar gas flow maintained. The same procedure was adopted to synthesize the lateral structures except that we use a shadow mask to partially cover the as-grown $(BA)_2PbI_4$ ($(BA)_2PbBr_4$ and $(PEA)_2PbI_4$) plates to prevent them from being contacted with MACl (MAI) vapor. By simply prolonging the reaction time to 30 min, the multiheterostructures can be obtained.

Powder X-ray spectrum measurements were carried out using Bruker D2 PHPSER (Cu Kα λ = 0.15419 nm, nickel filter, 25 kV, 40 mA). Optical microscopy images were acquired by a Mshot-MJ30 optical microscope. The SEM images were collected on a JEOL 7001F field-emission scanning electron microscope and EDX spectra and mapping were performed using the same SEM equipped with EDX detector.

Absorption and Photoluminescence Spectroscopy. The absorption spectra were recorded on a UV−Vis spectrophotometer (UV-1750, SHIMADZU). The photoluminescence measurements were performed in backscattering configuration using a Horiba HR800 system equipped with a 100 g/mm excited by a 442 nm He−Cd laser with a power of 1 μW or a 355 nm DSSP laser with a power of 5 μW.

Electrical Measurements. 5 nm Cr/50 nm Au electrodes were defined by a shadow mask and deposited by electron beam evaporation. The output ($I-V$) curves were measured in a probe station coupled to a Keithley 4200.

■ ASSOCIATED CONTENT

Ⓢ Supporting Information

The Supporting Information is available free of charge on the ACS Publications website at DOI: 10.1021/acs.jpclett.7b02843.

> Schematic illustration of the solution process for obtaining N = 1 2D perovskite. Optical images of perovskite plates before intercalation. Optical image of electronic devices. SEM and EDS of N = 1 perovskite. Time evolution of SEM images of heterostructures. PL spectra of N = 1 and N = 2 plates synthesized by solution method. PL spectra of lateral and vertical heterostructures to indicate the intensity quenching. PL spectra of heterostructures after device fabrication. PL spectra and XRD date of multiheterostructures. $I-V$ curves for N = 1 and N = 2 plates. (PDF)

■ AUTHOR INFORMATION

Corresponding Authors

*J.Z.: Email: zhangjwill@semi.ac.cn.
*D.L.: Email: dehuili@hust.edu.cn.

ORCID

Qinghai Tan: 0000-0003-4808-4795
Jianbing Zhang: 0000-0003-0642-3939
Jianfeng Zang: 0000-0002-1775-4605
Pingheng Tan: 0000-0001-6575-1516
Jun Zhang: 0000-0002-9831-6796
Dehui Li: 0000-0002-5945-220X

Author Contributions

#J.W. and J.L. contributed to this work equally.

Notes

The authors declare no competing financial interest.

■ ACKNOWLEDGMENTS

D.L. acknowledges the support from NSFC (61674060) and the Fundamental Research Funds for the Central Universities, HUST (2017KFYXJJ030, 2017KFXKJC003, 2017KFXKJC003). J.Zhang. acknowledges the support from National Basic Research Program of China (2016YFA0301200, 2017YFA0303401) and NSFC (11574305, 51527901). D.L. and J.Zhang. acknowledge the support from National Young 1000 Talent Plan of China.

■ REFERENCES

(1) Nie, W. Y.; Tsai, H.; Asadpour, R. J.; Blancon, C.; Neukirch, A. J.; Gupta, G.; Crochet, J. J.; Chhowalla, M.; Tretiak, S.; Alam, M. A.; et al. High-efficiency solution-processed perovskite solar cells with millimeter-scale grains. *Science* **2015**, *347*, 522−525.

(2) Li, W.; Wang, Z.; Deschler, F.; Gao, S.; Friend, R. H.; Cheetham, A. K. Chemically diverse and multifunctional hybrid organic−inorganic perovskites. *Nat. Rev. Mater.* **2017**, *2*, 16099.

(3) Li, D. H.; Wang, G. M.; Cheng, H.-C.; Chen, C.-Y.; Wu, H.; Liu, Y.; Huang, Y.; Duan, X. F. Size-dependent phase transition in methylammonium lead iodide perovskite microplate crystals. *Nat. Commun.* **2016**, *7*, 11330.

(4) Green, M. A.; Ho-Baillie, A.; Snaith, H. J. The emergence of perovskite solar cells. *Nat. Photonics* **2014**, *8*, 506−514.

(5) Shi, D.; Adinolfi, V.; Comin, R.; Yuan, M. J.; Alarousu, E.; Buin, C.; Chen, Y.; Hoogland, S.; Rothenberger, A.; Katsiev, K.; et al. Low trap-state density and long carrier diffusion in organolead trihalide perovskite single crystals. *Science* **2015**, *347*, 519−522.

(6) Johnston, M. B.; Herz, L. M. Hybrid perovskites for photovoltaics: Charge-carrier recombination, diffusion, and radiative efficiencies. *Acc. Chem. Res.* **2016**, *49*, 146−154.

(7) Xing, G.; Mathews, N.; Lim, S. S.; Yantara, N.; Liu, X.; Sabba, D.; Grätzel, M.; Mhaisalkar, S.; Sum, T. C. Low-temperature solution-processed wavelength-tunable perovskites for lasing. *Nat. Mater.* **2014**, *13*, 476−480.

(8) Xiao, Z.; Kerner, R. A.; Zhao, L.; Tran, N. L.; Lee, K. M.; Koh, T.-W.; Scholes, G. D.; Rand, B. P. Efficient perovskite light-emitting diodes featuring nanometre-sized crystallites. *Nat. Photonics* **2017**, *11*, 108−115.

(9) Li, X.; Dar, M. I.; Yi, C.; Luo, J.; Tschumi, M.; Zakeeruddin, S. M.; Nazeeruddin, M. K.; Han, H.; Grätzel, M. Improved performance and stability of perovskite solar cells by crystal crosslinking with alkylphosphonic acid ω-ammonium chlorides. *Nat. Chem.* **2015**, *7*, 703−711.

(10) Chiang, C. H.; Nazeeruddin, M. K.; Grätzel, M.; Wu, C. G. The synergistic effect of H_2O and DMF towards stable and 20% efficiency inverted perovskite solar cells. *Energy Environ. Sci.* **2017**, *10*, 808−817.

(11) Cao, D. H.; Stoumpos, C. C.; Farha, O. K.; Hupp, J. T.; Kanatzidis, M. G. 2D homologous perovskites as light-absorbing materials for solar cell applications. *J. Am. Chem. Soc.* **2015**, *137*, 7843−7850.

(12) Tsai, H.; Nie, W.; Blancon, J.-C.; Stoumpos, C. C.; Asadpour, R.; Harutyunyan, B.; Neukirch, A. J.; Verduzco, R.; Crochet, J. J.; Tretiak, S.; et al. High-efficiency two-dimensional Ruddlesden-Popper perovskite solar cells. *Nature* **2016**, *536*, 312−316.

(13) Stoumpos, C. C.; Cao, D. H.; Clark, D. J.; Young, J.; Rondinelli, J. M.; Jang, J. I.; Hupp, J. T.; Kanatzidis, M. G. Ruddlesden−Popper hybrid lead iodide perovskite 2D homologous semiconductors. *Chem. Mater.* **2016**, *28*, 2852−2867.

(14) Yuan, M.; Quan, L. N.; Comin, R.; Walters, G.; Sabatini, R.; Voznyy, O.; Hoogland, S.; Zhao, Y.; Beauregard, E. M.; Kanjanaboos, P.; et al. Perovskite energy funnels for efficient light-emitting diodes. *Nat. Nanotechnol.* **2016**, *11*, 872−877.

(15) Tan, Z.; Wu, Y.; Hong, H.; Yin, J.; Zhang, J.; Lin, L.; Wang, M.; Sun, X.; Sun, L.; Huang, Y.; et al. Two-Dimensional $(C_4H_9NH_3)_2PbBr_4$ perovskite crystals for high-performance photodetector. *J. Am. Chem. Soc.* **2016**, *138*, 16612−16615.

(16) Ha, S.-T.; Shen, C.; Zhang, J.; Xiong, Q. H. Laser cooling of organic−inorganic lead halide perovskites. *Nat. Photonics* **2015**, *10*, 115−121.

(17) Smith, I. C.; Hoke, E. T.; Solis-Ibarra, D.; McGehee, M. D.; Karunadasa, H. I. A layered hybrid perovskite solar-cell absorber with enhanced moisture stability. *Angew. Chem., Int. Ed.* **2014**, *53*, 11232−11235.

(18) Lauhon, L. J.; Gudiksen, M. S.; Wang, D.; Lieber, C. M. Epitaxial core-shell and core-multishell nanowire heterostructures. *Nature* **2002**, *420*, 57−61.

(19) Alivisatos, A. P. Semiconductor clusters, nanocrystals, and quantum dots. *Science* **1996**, *271*, 933−937.

(20) Liu, Y.; Weiss, N. O.; Duan, X. F.; Cheng, H. C.; Huang, Y.; Duan, X. F. Van der Waals heterostructures and devices. *Nat. Rev. Mater.* **2016**, *1*, 16042.

(21) Voznyy, O.; Sutherland, B. R.; Ip, A. H.; Zhitomirsky, D.; Sargent, E. H. Engineering charge transport by heterostructuring solution-processed semiconductors. *Nat. Rev. Mater.* **2017**, *2*, 17026.

(22) Sulpizio, J. A.; Ilani, S.; Irvin, P.; Levy, J. Nanoscale phenomena in oxide heterostructures. *Annu. Rev. Mater. Res.* **2014**, *44*, 117−149.

(23) Reiss, P.; Protiere, M.; Li, L. Core/shell semiconductor nanocrystals. *Small* **2009**, *5*, 154−168.

(24) Geim, A. K.; Grigorieva, I. V. Van der Waals heterostructures. *Nature* **2013**, *499*, 419−425.

(25) Yu, W. J.; Li, Z.; Zhou, H.; Chen, Y.; Wang, Y.; Huang, Y.; Duan, X. F. Vertically stacked multi-heterostructures of layered materials for logic transistors and complementary inverters. *Nat. Mater.* **2012**, *12*, 246−252.

(26) Georgiou, T.; Jalil, R.; Belle, B. D.; Britnell, L.; Gorbachev, R. V.; Morozov, S. V.; Kim, Y.-J.; Gholinia, A.; Haigh, S. J.; Makarovsky, O.; et al. Vertical field-effect transistor based on graphene-WS2 heterostructures for flexible and transparent electronics. *Nat. Nanotechnol.* **2012**, *8*, 100−103.

(27) Holonyak, N.; Kolbas, R.; Dupuis, R.; Dapkus, P. Quantum-well heterostructure lasers. *IEEE J. Quantum Electron.* **1980**, *16*, 170−186.

(28) Gopinadhan, K.; Shin, Y. J.; Jalil, R.; Venkatesan, T.; Geim, A. K.; Neto, A. H.; Yang, H. Extremely large magnetoresistance in few-layer graphene/boron−nitride heterostructures. *Nat. Commun.* **2015**, *6*, 8337.

(29) Oh, N.; Kim, B. H.; Cho, S. Y.; Nam, S.; Rogers, S. P.; Jiang, Y.; Flanagan, J. C.; Zhai, Y.; Kim, J. H.; Lee, J.; et al. Double-heterojunction nanorod light-responsive LEDs for display applications. *Science* **2017**, *355*, 616−619.

(30) Yan, R.; Gargas, D.; Yang, P. D. Nanowire photonics. *Nat. Photonics* **2009**, *3*, 569−576.

(31) Novoselov, K. S.; Mishchenko, A.; Carvalho, A.; Neto, A. H. C. 2D materials and van der Waals heterostructures. *Science* **2016**, *353*, aac9439.

(32) Li, M.-Y.; Shi, Y.; Cheng, C.-C.; Lu, L.-S.; Lin, Y.-C.; Tang, H.-L.; Tsai, M.-L.; Chu, C.-W.; Wei, K.-H.; He, J.-H.; Chang, W.-H.; et al. Epitaxial growth of a monolayer WSe_2-MoS_2 lateral p−n junction with an atomically sharp interface. *Science* **2015**, *349*, 524−528.

(33) Wang, G.; Li, D. H.; Cheng, H. C.; Li, Y.; Chen, C. Y.; Yin, A.; Zhao, Z.; Lin, Z.; Wu, H.; He, Q.; et al. Wafer-scale growth of large arrays of perovskite microplate crystals for functional electronics and optoelectronics. *Sci. Adv.* **2015**, *1*, e1500613.

(34) Ha, S. T.; Liu, X.; Zhang, Q.; Giovanni, D.; Sum, T. C.; Xiong, Q. Synthesis of organic-inorganic lead halide perovskites nanoplatelets: towards high performance perovskites solar cells and optoelectronic devices. *Adv. Opt. Mater.* **2014**, *2*, 838.

(35) Zhang, Q.; Ha, S. T.; Liu, X.; Sum, T. C.; Xiong, C. Room-Temperature near-infrared high-Q perovskite whispering-gallery planar nanolasers. *Nano Lett.* **2014**, *14*, 5995−6001.

(36) Stoumpos, C. C.; Soe, C. M. M.; Tsai, H.; Nie, W.; Blancon, J.; Cao, D. H.; Liu, F.; Traore, B.; Katan, C.; Even, J.; Mohite, A. D.; Kanatzidis, M. G. High members of the 2D Ruddlesden-Popper halide perovskites: synthesis, optical properties, and solar cells of $(CH_3(CH_2)_3NH_3)_2(CH_3NH_3)_4Pb_5I_{16}$. *Chem.* **2017**, *2*, 427−440.

(37) Ishihara, T.; Takahashi, J.; Goto, T. Optical properties due to electronic transitions in two-dimensional semiconductors $(C_nH_{2n+1}NH_3)_2PbI_4$. *Phys. Rev. B: Condens. Matter Mater. Phys.* **1990**, *42*, 11099−11107.

(38) Christodoulou, S.; Rajadell, F.; Casu, A.; Vaccaro, G.; Grim, J. Q.; Genovese, A.; Manna, L.; Climente, J. I.; Meinardi, F.; Rain, G.; et al. Band structure engineering via piezoelectric fields in strained anisotropic CdSe/CdS nanocrystals. *Nat. Commun.* **2015**, *6*, 7905.

(39) Li, D. H.; Liu, Y.; de la Mata, M.; Magen, C.; Arbiol, J.; Feng, Y.; Xiong, Q. H. Strain induced spatially indirect excition recombination in zinc-blende/wurtzite CdS heterostructures. *Nano Res.* **2015**, *8*, 3035.

(40) Splendiani, A.; Sun, L.; Zhang, Y.; Li, T.; Kim, J.; Chim, C. Y.; Galli, G.; Wang, F. Emerging photoluminescence in monolayer MoS_2. *Nano Lett.* **2010**, *10*, 1271−1275.

(41) Chen, H.-S.; Yeh, D.-M.; Lu, Y.-C.; Chen, C.-Y.; Huang, C.-F.; Tang, T.-Y.; Yang, C. C.; Wu, C.-S.; Chen, C.-D. Strain relaxation and quantum confinement in InGaN/GaN nanoposts. *Nanotechnology* **2006**, *17*, 1454−1458.

(42) Hong, X.; Kim, J.; Shi, S.; Zhang, Y.; Jin, C.; Sun, Y.; Tongay, S.; Wu, J.; Zhang, Y.; Wang, F. Ultrafast charge transfer in atomically thin MoS_2/WS_2 heterostructures. *Nat. Nanotechnol.* **2014**, *9*, 682−686.

(43) Ceballos, F.; Bellus, M. Z.; Chiu, H. Y.; Zhao, H. Ultrafast charge separation and indirect exciton formation in a MoS_2-$MoSe_2$ van der Waals heterostructure. *ACS Nano* **2014**, *8*, 12717−12724.

(44) Kozawa, D.; Carvalho, A.; Verzhbitskiy, I.; Giustiniano, F.; Miyauchi, Y.; Mouri, S.; Castro Neto, A. H.; Matsuda, K.; Eda, G. Evidence for fast interlayer energy transfer in $MoSe_2/WS_2$ heterostructures. *Nano Lett.* **2016**, *16*, 4087−4093.

(45) Liu, J.; Leng, J.; Wu, K.; Zhang, J.; Jin, S. Y. Observation of internal photoinduced electron and hole separation in hybrid two-dimensional perovskite films. *J. Am. Chem. Soc.* **2017**, *139*, 1432−1435.

(46) Li, L.; Sun, Z.; Wang, P.; Hu, W.; Wang, S.; Ji, C. M.; Hong, M. C.; Luo, J. H. Tailored engineering of an unusual $(C_4H_9NH_3)_2(CH_3NH_3)_2Pb_3Br_{10}$ two-dimensional multilayered perovskite ferroelectric for high performance photodetectors. *Angew. Chem.* **2017**, *129*, 12318−12322.

(47) Dou, L.; Wong, A. B.; Yu, Y.; Lai, M.; Kornienko, N.; Eaton, S. W.; Fu, A.; Bischak, C. G.; Ma, J.; Ding, T.; et al. Atomically thin two-dimensional organic-inorganic hybrid perovskites. *Science* **2015**, *349*, 1518−1521.

(48) Gan, X.; Wang, O.; Liu, K.; Du, X.; Guo, L.; Liu, H. X. 2D homologous organic-inorganic hybrids as light-absorbers for planer and nanorod-based perovskite solar cells. *Sol. Energy Mater. Sol. Cells* **2017**, *162*, 93−102.

(49) Blancon, J. C.; Tsai, H.; Nie, W.; Stoumpos, C. C.; Pedesseau, L.; Katan, C.; Kepenekian, M.; Soe, C. M. M.; Appavoo, K.; Sfeir, M. Y.; et al. Extremely efficient internal exciton dissociation through edge states in layered 2D perovskites. *Science* **2017**, *355*, 1288.

(50) Giordano, F.; Abate, A.; Pablo, J.; Baena, J. P. C.; Saliba, M.; Matsui, T.; Im, S. H.; Zakeeruddin, S. M.; Nazeeruddin, M. K.; Hagfeldt, A.; et al. One-Year stable perovskite solar cells by 2D/3D interface engineering. *Nat. Commun.* **2016**, *7*, 10379.

(51) Wang, Z.; Lin, Q.; Chmiel, F. P.; Sakai, N.; Herz, L. M.; Snaith, H. J. Efficient ambient-air-stable solar cells with 2D−3D heterostructured butylammonium-caesium-formamidinium lead halide perovskites. *Nat. Energy* **2017**, *2*, 17135.

DOI: 10.1021/acs.jpclett.7b02843
J. Phys. Chem. Lett. 2017, 8, 6211−6219